Direct Numerical Simulation of the Turbulent Flow in a Baffled Tank Driven by a Rushton Turbine

J. J. J. Gillissen and H. E. A. Van den Akker
Dept. of Chemical Engineering, Delft University of Technology, Leeghwaterstraat 39, 2628 CB Delft, the Netherlands

DOI 10.1002/aic.13762
Published online March 12, 2012 in Wiley Online Library (wileyonlinelibrary.com).

We present a direct numerical simulation (DNS) of the turbulent flow in a baffled tank driven by by a Rushton turbine. The DNS is compared to a Large Eddy Simulation (LES), a Reynolds Averaged Navier-Stokes (RANS) simulation, Laser Doppler Velocimetry data, and Particle Image Velocimetry data from the literature. By Reynolds averaging the DNS-data, we validate the turbulent viscosity hypothesis by demonstrating strong alignment between the Reynolds stress and the mean strain rate. Although the turbulent viscosity ν_T *in the DNS is larger than in the RANS simulation, the turbulent viscosity parameter* $C_\mu = \nu_T\epsilon/k^2$*, is an order of magnitude smaller than the standard 0.09 value of the k-*ϵ *model. By filtering the DNS-data, we show that the Smagorinsky constant* C_S *is uniformly distributed over the tank with* $C_S \approx 0.1$*. Consequently, the dynamic Smagorisnky model does not improve the accuracy of the LES.* © 2012 American Institute of Chemical Engineers *AIChE J,* 58: 3878–3890, 2012

Keywords: computational fluid dynamics, fluid mechanics, mathematical modeling, mixing, turbulence

Introduction

Because of their widespread application in the (bio-)chemical industries, the fluid dynamics of stirred tanks (STs) operated in the turbulent flow regime is subject of a vast amount of literature, (see eg., Refs. 1–6). However, a complete and reliable picture of the flow is still lacking due to the broad range of time and length scales which is typical of the turbulent flow regime. Length scales range from turbine (blade) size down to the Kolmogorov length scale, which often is in the submillimeter range. As a result, acquiring a fully resolved picture of the turbulent flow field has been impossible so far.

For engineering purposes, these days computational fluid dynamics (CFD) simulations are routinely being used for analyzing and optimizing problems in ST's (see eg., Refs. 7,8). Rather than resolving the turbulent flow field, engineering CFD resorts to modeling the effect of the turbulent eddies on the average flow field. This so-called Reynolds averaged Navier–Stokes (RANS) approach now acts as the work horse for engineering CFD. The RANS technique involves solving the mean flow only and adopting a model to incorporate the effects of the turbulent fluctuations (see eg., Ref. 9). On the analogy of molecular momentum transport, the effect of the fluctuations is usually modeled by means of an additional viscous stress. In spite of its simplicity, this so-called turbulent viscosity model reproduces remarkably accurate predictions of the averaged flow field, not only for simple flow problems, but also for more complex, practical problems such as the ST flow (see eg., Ref. 6). In general, however, turbulence levels in ST flow are underpredicted by RANS.[10,6]

When chemical reaction rates or the rates of physical transformation processes are slow compared to the turbulent frequencies, RANS is a valuable tool in chemical reactor engineering. On the contrary, when the time scales of the chemical or physical operations are comparable to or smaller than the turbulent time scales, the chemical conversion strongly depends on the details of the turbulence. For these cases, the computed chemical conversion heavily relies on the modeling of the fluctuations, which is by no means reliable. Then, RANS provides very little insight in the process of interest. Such issues demand a more detailed computational approach.[11]

Compared to RANS, a more sophisticated approach is the so-called large eddy simulations (LES) in which a substantial part of the turbulent energy spectrum is explicitly calculated (see eg., Ref. 12). As compared to RANS, where the complete spectrum of turbulence is modeled, LES only models the effect of the high frequency part of the spectrum, that is, of the eddies smaller than the grid spacing, by some so-called subgrid-scale model. As the low frequency part is computed directly, LES provides significantly more detail and is more suitable when specific turbulence characteristics are important. In the case of chemical conversion processes, LES offers good results when the reaction rates lie in the frequency range of the resolved energy spectrum. Because of the smaller energy content and the more universal behavior, modeling the high frequency part is less critical and less complicated when compared to the low frequency part. For flows unaffected by walls, such as jets, LES is a powerful tool to

Correspondence concerning this article should be addressed to J. J. J. Gillissen at j.j.j.gillissen@tudelft.nl.

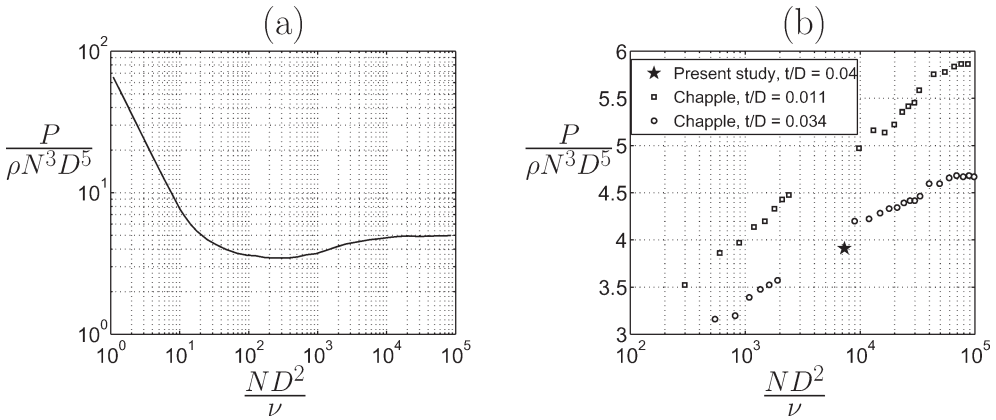

Figure 1. (a) Power number vs. Reynolds number. Data are taken from Ref. 19. (b) Power number vs Reynolds number. Comparison of DNS1 to the experimental data of Ref. 27.

predict turbulent mixing and associated chemical reaction rates (see, eg., Ref. 13). In principle, problems arise when interactions with solid walls are important. Close to walls the assumptions underlying LES break down due to the anisotropic and nonequilibrium nature of the near-wall turbulence. To compute high Reynolds number flows over solid walls, LES models may have to be supplemented with wall models, providing modified boundary conditions based on flat plate boundary layer theory or on RANS solutions of the near-wall layer.[14]

Both the RANS and LES approaches imply a loss of information and render the CFD results approximate. Validation by means of experimental data, such as those obtained in Refs. 3,5 is therefore indispensable. In addition to comparing to experiments, RANS and LES can also be validated by comparing to direct numerical simulation (DNS), that is, a computational simulation without any modeling that fully resolves all length scales of the turbulent flow field. As all turbulent eddies are fully resolved without any modeling, DNS has the potential of replacing the role of the experiment in providing reference data for both RANS and LES. Turning to DNS seems to be a logical step in the process of developing CFD techniques into a versatile tool. So far, however, performing a DNS of the turbulent flow inside a ST with baffles has still been undoable for industrially relevant operating conditions, due to limitations in computational resources. The dazzling growth in computational power, however, is gradually bringing DNS of turbulent flow in a ST within reach.

DNS of ST flow at $Re = 7275$ has previosuly been reported in Refs. 15,16 Here, the Reynolds number

$$Re = \frac{ND^2}{v}, \tag{1}$$

has been defined in terms of the turbine diameter D, the turbine frequency N and the fluid kinematic viscosity v. As the grid spacing was several orders of magnitude larger than the Kolmogorov scale, these calculation would better be classified as LES without a subgrid model. Fully resolved DNS for an unbaffled ST at $Re = 1042$ was reported in Refs. 17,18 This value of Re, however, is significantly below the fully turbulent regime as indicated in Figure 1a by a Re-independent Power number Po for $Re \gtrsim 2 \times 10^4$. Here

$$Po = \frac{P}{\rho N^3 D^5}, \tag{2}$$

with P and ρ denoting the power draw and the fluid mass density, respectively.

Around 1990 our Delft research group got involved in CFD of turbulent ST flow; our first paper on RANS being that due to Bakker and Van den Akker.[2] Soon thereafter, we simulated ST flow using an in-house LES code on the basis of a lattice-Boltzmann (LB) technique.[4] In the present work, we take the next step in this long-way process of reducing and eventually eliminating turbulence models. We now report about a DNS of a standard ST geometry (including baffles) at a Reynolds number of $Re = 7300$. A total of $\approx 2.9 \times 10^9$ grid points are used inside the tank.

It is noted that, according to Figure 1a, this Reynolds number is closer to, but not yet within, the fully turbulent (Re-independent) regime, which is generally considered as: $Re \gtrsim 2 \times 10^4$. This means that at $Re = 7300$, the flow is not fully turbulent over the whole domain. However, as we will see, the flow is fully turbulent close to the turbine, where most of the mixing occurs. Another point of caution is that, in the present DNS, the minimum Kolmogorov length scale is somewhat smaller than the grid spacing. Therefore, we are not certain whether the present DNS fully resolves the smallest eddies, and what the effect of this under-resolution is on the predicted flow patterns. Despite this uncertainty, we feel that this work is a serious step toward a fully resolved picture of the turbulent flow in a ST.

Our primary motivation for generating the DNS-data is to asses the fundamental assumptions underlying LES and RANS. By Reynolds averaging the DNS-data, we will study the structure of the Reynolds stress. We will assess the turbulent viscosity hypothesis which provides guidelines for improving RANS models of ST flow. Furthermore by spatially filtering the DNS-data, we will explicitly calculate the energy flux from the large to the small scales, thereby obtaining the optimal value for the Smagorinsky constant, being the LES model parameter.

Mathematical Models

DNS

DNS is governed by the incompressible Navier–Stokes equations

$$\nabla \cdot \boldsymbol{u} = 0, \quad \frac{\partial \boldsymbol{u}}{\partial t} = \nabla \cdot \left(-\boldsymbol{uu} - \frac{p}{\rho}\boldsymbol{\delta} + 2v\boldsymbol{S} \right), \tag{3}$$

subjected to the no-slip boundary condition on the tank wall and the rotating turbine. Here, t is the time, ∇, nabla operator, $\boldsymbol{u}$, velocity, ρ, mass density, p, pressure, $\boldsymbol{S} = \frac{1}{2}[\nabla \boldsymbol{u} + (\nabla \boldsymbol{u})^T]$, rate of strain tensor, $\boldsymbol{\delta}$, unit tensor, ν, kinematic viscosity

RANS

In RANS simulations, only the Reynolds averaged part of the flow is numerically being solved, while the fluctuating part is modeled (see, eg., Ref. 9). The RANS equations are obtained by applying the so-called Reynolds averaging operator $\overline{\cdots}$ to Eq. 3

$$\nabla \cdot \overline{\boldsymbol{u}} = 0, \quad \frac{\partial \overline{\boldsymbol{u}}}{\partial t} = \nabla \cdot \left(-\overline{\boldsymbol{u}}\,\overline{\boldsymbol{u}} - \frac{\overline{p}}{\rho}\boldsymbol{\delta} + 2\nu\overline{\boldsymbol{S}} + \boldsymbol{R} \right). \tag{4}$$

Eq. 4 describe the Reynolds averaged velocity $\overline{\boldsymbol{u}}$ and the Reynolds averaged pressure $\overline{p}$. These equations are similar to Eq. 3, except for one additional stress term $\boldsymbol{R}$, which represents the effects of the fluctuating part of the flow on the mean part of flow and is referred to as the Reynolds stress

$$\boldsymbol{R} = -\overline{\boldsymbol{u}\boldsymbol{u}} + \overline{\boldsymbol{u}}\,\overline{\boldsymbol{u}} = -\overline{\boldsymbol{u}'\boldsymbol{u}'}, \tag{5}$$

where $\boldsymbol{u}'$ denotes the fluctuating part of $\boldsymbol{u}$. The appearance of $\boldsymbol{R}$ introduces more unknowns than equations and this quantity has to be modeled to obtain a closed set of equations.

In this article, we consider the most commonly used $k-\epsilon$ model, in which $\boldsymbol{R}$ is replaced by a viscous stress

$$\boldsymbol{R} = 2\nu_T\overline{\boldsymbol{S}}, \quad \nu_T = C_\mu \frac{k^2}{\epsilon}. \tag{6}$$

The turbulent viscosity ν_T is expressed in terms of the turbulent kinetic energy $k = \frac{1}{2}\overline{|\boldsymbol{u}'|^2}$ and the turbulent energy dissipation rate $\epsilon = 2\nu\overline{|\boldsymbol{S}'|^2}$, for which additional phenomenological equations have to be solved.

There is no universally optimal value for the turbulent viscosity parameter C_μ. The commonly used value $C_\mu = 0.09$ is based on experimental data in the turbulent boundary layer.

LES

In large eddy simulation (LES), both the mean flow as well as the low wavenumber part of the turbulent spectrum are resolved, while the high wavenumber part is modeled (see, eg., Ref. 12). The LES equations are obtained by applying the so-called grid filter $\widetilde{\cdots}$ to Eq. 3. A grid filtered quantity $\widetilde{q}$ is defined as the average of q over one grid volume Δ^3, where Δ is the grid spacing. Applying $\widetilde{\cdots}$ to Eq. 3 provides equations for the grid filtered velocity $\widetilde{\boldsymbol{u}}$ and the grid filtered pressure $\widetilde{p}$

$$\nabla \cdot \widetilde{\boldsymbol{u}} = 0, \quad \frac{\partial \widetilde{\boldsymbol{u}}}{\partial t} = \nabla \cdot \left(-\widetilde{\boldsymbol{u}}\widetilde{\boldsymbol{u}} - \frac{\widetilde{p}}{\rho}\boldsymbol{\delta} + 2\nu\widetilde{\boldsymbol{S}} + \boldsymbol{\sigma} \right). \tag{7}$$

These equations are similar to Eq. 3, except for one additional stress term $\boldsymbol{\sigma}$, which represents the effects of the unresolved, high wavenumber scales on the resolved low wavenumber scales and is referred to as the subfilter stress

$$\boldsymbol{\sigma} = -\widetilde{\boldsymbol{u}\boldsymbol{u}} + \widetilde{\boldsymbol{u}}\widetilde{\boldsymbol{u}}. \tag{8}$$

The appearance of $\boldsymbol{\sigma}$ introduces more unknowns than equations and this quantity has to be modeled to obtain a closed set of equations. In this article, we adopt the most commonly used model developed by Smagorinsky, who expressed $\boldsymbol{\sigma}$ as a viscous stress and obtained an expression for the so-called Smagorinsky viscosity ν_e by assuming a balance between energy production and dissipation of the subfilter scales[20]

$$\boldsymbol{\sigma} = 2\nu_e\widetilde{\boldsymbol{S}}, \quad \nu_e = C_S^2\Delta^2|\widetilde{\boldsymbol{S}}|. \tag{9}$$

Here, C_S is the Smagorinsky constant, whose value must be tuned to obtain optimal results for a given flow problem and grid resolution.

The optimal value for C_S depends on the type of flow. For instance, $C_S \approx 0.23$ for isotropic turbulence and $C_S \approx 0.1$ for turbulent channel flow.[21] For ST flow the optimal value for C_S has not yet been determined. In a previously reported LES of a ST flow, Hartmann et al.[6] arbitrarily used $C_S = 0.12$. Germano et al.[21] proposed a method to dynamically compute the optimal value for C_S, which in general is space and time dependent. This method involves a second, so-called test filter $\widehat{\cdots}$. A test filtered quantity $\widehat{q}$ is defined as the average of q over a volume with a linear dimension Δ_f, which is larger than the grid spacing Δ.

The optimal Smagorinsky constant is obtained by equating the right hand sides of Eqs. 8 and 9, taking the double inner product of the result with $\widehat{\widetilde{\boldsymbol{S}}}$ and applying the Reynolds average $\overline{\cdots}$[21]

$$C_S^2 = \frac{\overline{(-\widehat{\widetilde{\boldsymbol{u}}\widetilde{\boldsymbol{u}}} + \widehat{\widetilde{\boldsymbol{u}}}\widehat{\widetilde{\boldsymbol{u}}}) : \widehat{\widetilde{\boldsymbol{S}}}}}{\Delta_f^2\overline{\widehat{\widetilde{\boldsymbol{S}}}^3}}. \tag{10}$$

The k in LES is composed of both resolved and unresolved scales and we use $k = \frac{1}{2}\overline{|\widetilde{\boldsymbol{u}}'|^2} + \overline{\left(\frac{C_S^2}{C_K}\Delta|\widetilde{\boldsymbol{S}}|\right)^2}$ to model k, where the model parameter is taken as $C_K = 0.05$.[22] Similarly, ϵ in LES consists of resolved and unresolved scales and is computed as $\epsilon = \overline{\widetilde{\boldsymbol{S}}' : (2\nu\widetilde{\boldsymbol{S}}' + \widetilde{\boldsymbol{\sigma}}')}$.

Numerical Setup

Geometry

We consider the flow inside a cylindrical, baffled tank, driven by a six-bladed Rushton turbine. The geometry is sketched in Figure 2. Both the top and the bottom of the tank are no-slip solid surfaces. For ready reference, we use identical parameters as in the laser doppler velocimetry (LDV) experiments of Schäfer et al.[3] The Reynolds number (Eq. 1) equals $Re = 7300$.

Methods

We use DNS and LES to compute numerical solutions of ST flow. An overview of the simulation parameters is given in Table 1. The DNS and LES solutions have been generated using our in-house LB (LB) code.[4] Details of this LB method can be found in Ref. 23 The advantages of the LB method are the low number of operations per grid node and time step, and the excellent performance on parallel computer platforms. Furthermore, our LB code uses a highly efficient method to deal with the no-slip boundary condition on the turbine and the baffled tank wall.[4] In this immersed boundary method, the no-slip surfaces are represented by a set of points. On each of these points, the no-slip condition is enforced by adding momentum sources to the nearby grid points. The resulting body force field $\boldsymbol{F}$ is defined such

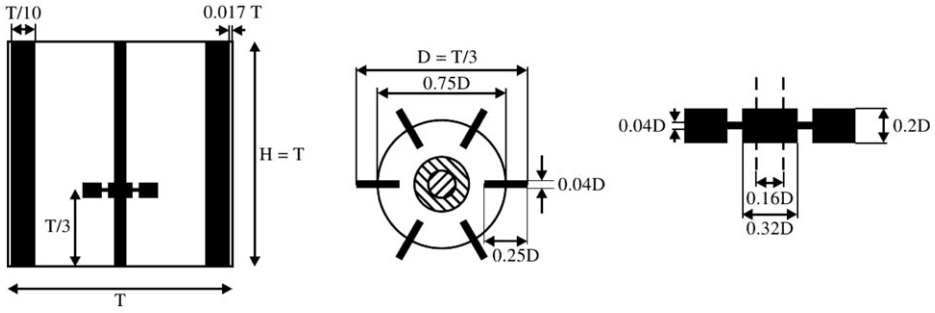

Figure 2. ST geometry. Pictures are taken from Ref. 6.

that it drives the fluid velocity on the solid surfaces to the no-slip velocity.

Our LB code uses a cubic and homogeneous grid. Grid refinement is achievable, although not implemented, by combining several cubic and homogeneous grids of different grid spacings, which involves a matching of the different solutions at the corresponding interfaces by means of interpolation.[24,25] Avoiding the associated interpolation errors, we do not follow such an approach, but simply use a single cubic and homogeneous grid. The inefficiency of using a uniform grid is compensated by the high efficiency per grid node, which makes the present LB method competitive with classical Navier–Stokes solvers on refined grids.

To determine whether the DNS resolves all relevant scales, we have conducted two DNS's of ST flow on two different grids, which are composed of 1536^3 and 1024^3 grid nodes, referred to as DNS1 and DNS2. Excluding the nodes residing outside the cylindrical domain, a total of 2.9×10^9 and 8.4×10^8 grid points are used in DNS1 and DNS2. The number of grid points per blade height are 102 and 68, respectively.

In addition to DNS, we have conducted two LES's of ST flow on 256^3 grids corresponding to 17 grid points per blade height. The simulations, referred to as LES1 and LES2, use different subgrid models. In LES1, we use the constant Smagorinsky subgrid model, using a value of $C_S = 0.12$, in agreement with the previously reported LES of ST flow.[6] In LES2 the Smagorinsky constant is dynamically computed with Eq. 10 using a top-hat filter for $\widehat{\cdots}$ with a width of $\Delta_f = 4\,\Delta$. In LES2 we also apply the Van Driest wall damping.[26] In his model, the C_S is multiplied by a damping factor to eliminate any unphysically large values of the Smagorinsky viscosity near the solid surfaces

$$C_S^2 = (1 - \exp(-y^+/26)) \frac{\overline{(-\widehat{\widehat{\boldsymbol{u}}\boldsymbol{u}} + \widehat{\widehat{\boldsymbol{u}}\boldsymbol{u}}) : \widehat{\widehat{\boldsymbol{S}}}}}{\Delta_f^2 \overline{\widehat{\widehat{S}}^3}}. \qquad (11)$$

Here, $y^+ = y\sqrt{\tau_w/\rho}/\nu$, where y equals the distance to the nearest point on the solid surface and τ_w is the wall shear stress on that point, which is calculated from the immersed boundary body force $\boldsymbol{F}$.

In addition to DNS and LES, we also consider a RANS simulation from the literature.[6] This simulation was conducted using the commercial fluid dynamics code CFX version 5.5.1. A finite volume discretization scheme was used to numerically solve a combination of the $k - \omega$ and the $k - \epsilon$ models, including wall functions. The simulation used a sliding grid technique that involves a co-rotating grid in the inner region and a static grid in the outer region. The structured grid consisted of 2.3×10^5 grid points, corresponding to ten grid points per blade height.

Computational load

Our LB code is written in FORTRAN and parallelized using MPI. DNS1 was performed on 128 IBM Power6, 4.7 GHz CPU's of the Dutch national supercomputer SARA. Each time step required 8 of computing time, resulting in 30 h computation time for 15,000 time steps corresponding to one turbine revolution.

Postprocessing

Starting from quiescent conditions a ST flow simulation requires approximately 100 turbine revolutions to develop to a statistically steady, turbulent state. This start-up was computed using LES on the 256^3 grid. After the flow had fully developed, the LES flow field was interpolated onto the 1024^3 DNS2 grid. DNS2 was run for 10 turbine revolutions after which the flow had adapted to the new grid and recovered a statistically steady state. Then, flow variables were averaged during 10 turbine revolutions. Subsequently, the DNS2 flow field was interpolated onto the 1536^3 DNS1 grid and DNS1 was run for 10 revolutions, after which statistics were collected during another 10 revolutions.

The results of this work are presented mainly in terms of Reynolds averages. The Reynolds averaged quantities are one-point statistics, which in a baffled ST are functions of four coordinates. Three of these coordinates describe the position relative to the turbine (see Figure 3) and the fourth defines the relative position to one of the baffles. Constructing accurate Reynolds averaged functions of four variables requires a large amount of timely separated samples, which requires a large simulation time. Our computational budget did not permit more than 20 turbine revolutions for DNS1, which was insufficient to construct accurate Reynolds averaged functions of four variables. To circumvent this problem, we have restricted our focus to the close vicinity of the turbine, as in this region the flow statistics are hardly affected by the relative position to the baffles. By ignoring this influence we reduce the number of coordinates from four to three, which significantly reduces the number of

Table 1. Overview of the Simulations: The Number of Grid Points in the *x*, *y*, and *z*-directions are All Equal to N_x

Name	SGS Model	N_x
DNS1	–	1536
DNS2	–	1024
LES1	Constant Smagorinsky	256
LES2	Dynamic Smagorinsky	256

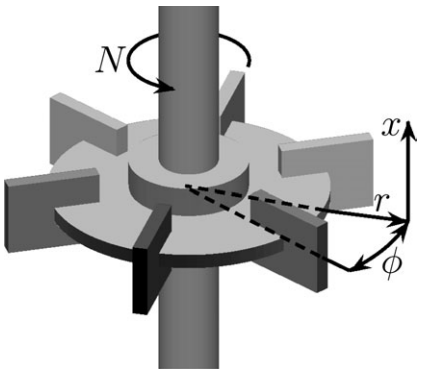

Figure 3. Coordinate system relative to the turbine.

samples required for obtaining accurate Reynolds averages. As sketched in Figure 3, these coordinates are the axial distance x to the turbine disk, the radial distance r to the turbine axis, and the downstream angle ϕ to the nearest turbine blade. In addition to Reynolds averaged values, a few results are presented in terms of phase averaged quantities, which is the average over ϕ of the corresponding Reynolds averaged quantity.

In all DNS and LES simulations, the time step based on the turbine tip velocity U_{tip} and grid spacing Δ is equal to $\Delta t U_{\text{tip}}/\Delta = 0.1$, which for DNS1 resulted in 1.6×10^4 time steps per turbine revolution. One-point statistics are computed over 10 revolutions by averaging the data from 1.6×10^3 instantaneous flow fields. In DNS1, two consecutive sampled fields are separated by a time interval of 100 Δt, or equivalently a 3.36° increment in the turbine angle. The statistical quantities are computed as functions of the cylindrical coordinates (x, r, ϕ) relative to the rotating turbine. As the turbine geometry has a periodicity of $\frac{\pi}{3}$ in ϕ, each field contains six realizations, we collect a total of 9.7×10^3 realizations from DNS1, which is sufficient for an accurate approximation of the first and the second order, one-point velocity statistics.

Results

Grid resolution

We evaluate the accuracy of DNS1 by comparing the results to DNS2, which is performed on a coarser grid resolution. Figure 5 shows the Reynolds averaged radial and azimuthal velocity components $\overline{u}_r$ and $\overline{u}_\phi$, the turbulent kinetic energy $k = \frac{1}{2}|\boldsymbol{u}'|^2$ and the turbulent energy dissipation rate ϵ as functions of the axial coordinate x for $\frac{r}{T} = \frac{1}{6}$ and $\phi = \frac{\pi}{4}$. This position, which is located at 15° behind the tip of the nearest turbine blade, as indicated with the dot in Figure 4a, corresponds to the maximum in k, and therefore, provides the most stringent evaluation of the adequacy of the computational grid. The axial profiles are drawn from $\frac{x}{T} = -0.1$ to 0.1, which corresponds to three blade heights. The data in Figure 5 show that the difference between DNS1 and DNS2 is ≈1% for $\overline{\boldsymbol{u}}$, ≈ 10% for k and ≈25% for ϵ. As DNS1 is performed on a finer grid than DNS2, these differences represent errors due to under-resolution in DNS2. To estimate the corresponding errors for DNS1, we would need to compare DNS1 to a simulation on an even finer grid. Unfortunately our computational budget did not allow this. Therefore, we can not exactly say whether DNS1 is grid independent or to what extend it is under-resolved. However, since DNS1 has a finer grid than DNS2, we can infer that the errors of DNS1 are smaller than the observed differences between DNS1 and DNS2, which are already rather small. It is further noted that the observed differences represent upper bounds, since Figure 5 focuses on the most turbulent spot in the tank. In other regions the differences are smaller.

To further study the grid resolution issue, we show in Figure 6 the Kolmogorov length scale $l_K = \nu^{3/4}\ \epsilon^{-1/4}$, in the ($\phi = \frac{\pi}{4}$)-plane which is located 15° behind the nearest turbine blade, as sketched in Figure 4b. The l_K attains a minimum value of 0.35Δ at $\frac{r}{T} = \frac{1}{6}$ and $\frac{x}{T} = \pm 0.02$, which suggest a somewhat under-resolved fluid velocity field.

Another way of evaluating the adequacy of the grid is by studying visualizations of the magnitude of the instantaneous vorticity $\boldsymbol{\omega} = \nabla \times \boldsymbol{u}$, which are shown in Figure 7. A logarithmic gray scale is used to properly visualize all the turbulent eddies, ranging from the turbine blade size down to the dissipating scales. The figure shows that the turbulence structures are smooth on all length scales, which suggests that the grid is adequate to resolve all the relevant scales.

This visualization further illustrates that the flow is fully turbulent near the impeller, where a wide range of length scales is observed. Further away from the impeller, the range is smaller, showing eddies of relatively large size, comparable to the blade size. This observation reflects that at $Re = 7300$ we are close to, but not within the fully turbulent regime, as indicated by a Re-independent power number for $Re \gtrsim 2 \times 10^4$, as sketched in Figure 1a.

Power number

Apart from offering a quantitative way of comparing to experimental data, the Power number (Eq. 2) also provides a

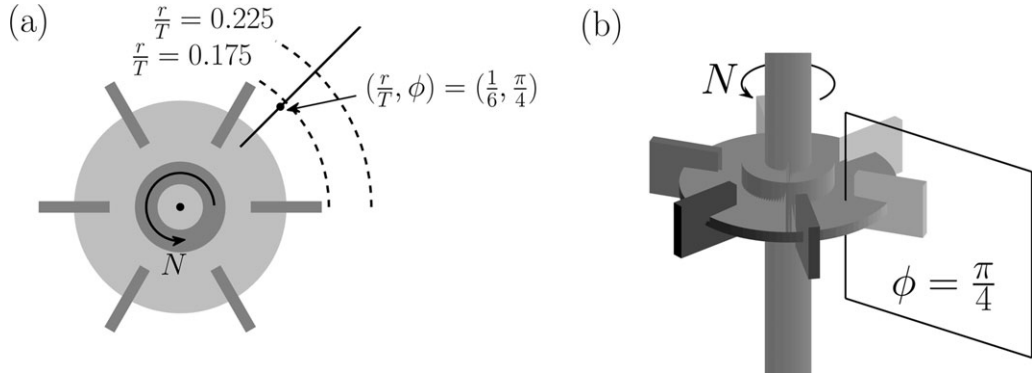

Figure 4. (a) The axial profiles in Figure 5 are located at the black dot. The phase averaged quantities in Figure 9 are obtained by averaging over the dashed lines. (b) The ($\phi = \frac{\pi}{4}$)-plane which is shown in Figures 6, 8, 10, 11, and 13.

check on the integral energy balance. Within our simulations, the flow is effectively driven by a body force field $\boldsymbol{F}$ that is used by the immersed boundary method to enforce the no-slip condition on the revolving and stationary surfaces. The Navier–Stokes equations (Eq. 3), including $\boldsymbol{F}$, can be manipulated into the integral energy equation, which constitutes a balance between the power P delivered by $\boldsymbol{F}$ and the viscous energy dissipation: $P = \int_V \boldsymbol{F} \cdot \boldsymbol{u} dV = \int_V 2\mu \boldsymbol{S} : \boldsymbol{S} dV$. In this balance, the energy dissipation is due to the deformation of the total velocity field, of both the mean flow and the turbulence, which differs from the turbulent energy dissipation ϵ which only involves the turbulence.

For DNS1, the Power number based on the immersed boundary forces field is $Po = 3.91$. This value seems rather small compared to $Po \approx 5$, which generally corresponds to fully turbulent conditions (see Figure 1a). Part of this discrepancy is due to our modest $Re = 7300$ which is somewhat below the fully turbulent regime for $Re \gtrsim 2 \times 10^4$. Another part is due to our relatively large blade thickness $t = 0.04\ D$. Both effects are illustrated in Figure 1b, showing good consistency between our numerical result and the torque measurements of Ref. 27 The Power number obtained from the integral energy dissipation equals $Po = 3.79$. There is a 3% difference between the integral energy dissipation and the power draw, which is rather satisfactory.

Comparison to experimental data

Figure 8 shows $\overline{\boldsymbol{u}}$ and k in the ($\phi = \frac{\pi}{4}$)-plane, comparing results from DNS1, LES1, RANS,[6] and LDV measurements.[3] Schäfer et al.[3] generated an extensive experimental data set for the validation of numerical simulations. They performed LDV measurements in a ST, by matching the refractive index of the liquid to that of the transparent material of turbine and vessel. The vessel height was $T = 0.15$ m, the rotational speed was $N = 44.5\ \mathrm{s}^{-1}$ and the working fluid was silicon oil, with a mass density of $\rho = 1.039 \times 10^3\ \mathrm{kg\ m}^{-3}$ and a kinematic viscosity of $\nu = 1.53 \times 10^{-5}\ \mathrm{m}^2\ \mathrm{s}^{-1}$. To our knowledge, these data are unique in comprising mean and fluctuating velocities in the turbine swept volume.

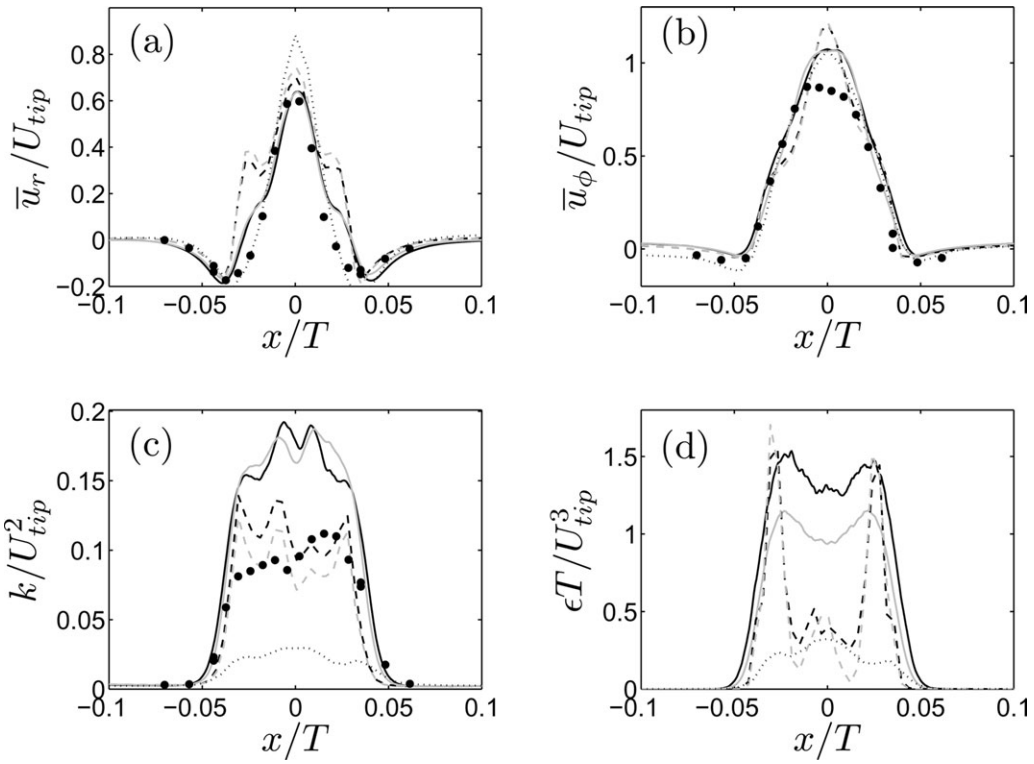

Figure 5. Comparison of Reynolds averaged radial velocity (a) azimuthal velocity (b), turbulent kinetic energy (c), and turbulent energy dissipation (d) at ($\frac{r}{T}$, ϕ) = ($\frac{1}{6}$, $\frac{\pi}{4}$), predicted by DNS1 (solid black lines), DNS2 (solid gray lines), LES1 (dashed black lines) LES2 (dashed black lines) RANS (dotted gray line lines), and LDV (data from Ref., 3 black dots).

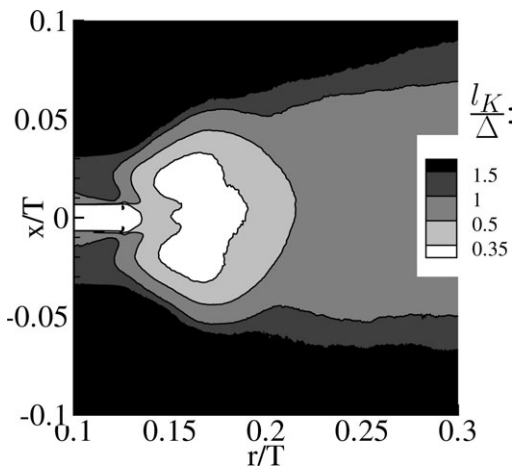

Figure 6. Kolmogorov length scale in the ($\phi = \frac{\pi}{4}$)-plane predicted by DNS1.

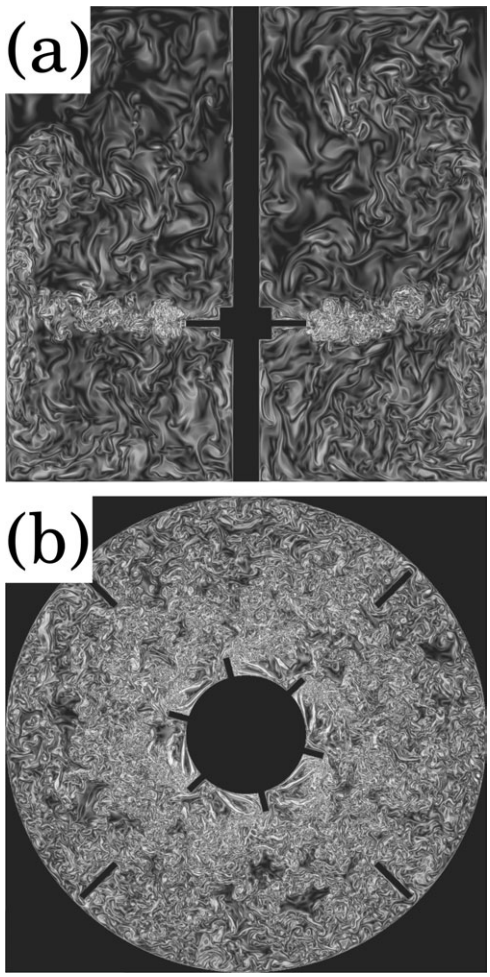

Figure 7. Instantaneous distribution of the vorticity magnitude predicted by DNS1 using a logarithmic gray scale in a plane that intersects the tank axis (a) and in the ($x = 0$)-plane (b).

The turbine rotates anti-clockwise.

The vector fields in Figure 8 show the fluid being axially drawn toward $x = 0$, and radially being pumped by the centrifugal action of the turbine. Furthermore, we observe two counter rotating vortices located at $(\frac{r}{T}, \frac{x}{T}) \approx (0.17, \pm 0.02)$. These so-called trailing vortices are emitted by the outer corners of the turbine blades and are responsible for a large portion of the mixing efficiency of the Rushton turbine.[1] In Figure 8, we indicate the cores of these vortices with the black dots. The agreement between simulation and experiment of the locations of the vortex cores is best for LES. The axial positions are slightly smaller for RANS and slightly larger for DNS.

Figure 8 also shows the distributions of k in the wake of the turbine blades, comparing the simulations to the LDV-data. Apparently the agreement, to the LDV is best for LES, while the peak value at $\frac{x}{T} = 0$ and $\frac{r}{T} \approx 0.17$ is two times larger for DNS and two times smaller for RANS. Further away from the turbine $\frac{r}{T} > 0.25$, all simulations agree within 10% to the LDV-data.

The differences between the simulations and the LDV-data are clearly demonstrated in Figure 5, showing the axial profiles of $\overline{\boldsymbol{u}}$ and k at the location of maximum k, being at $(\frac{r}{T}, \phi) = (\frac{1}{6}, \frac{\pi}{4})$. The comparison shows good agreement in $\overline{\boldsymbol{u}}$ between DNS, LES, RANS, and LDV. The results for k show that LES agrees best to LDV, while DNS is twice as large as LDV and RANS is twice as small as LDV.

Apart from Ref., 3 no other experimental data are available concerning the turbulent flow within the turbine swept volume. Outside the turbine swept volume other data are available, such as Ref., 28 obtained however at a larger $Re = 40{,}000$. We compare the simulations with these data in Figure 9(a), which shows axial profiles of the phase averaged k at $\frac{r}{T} = 0.175$. These profiles are obtained by averaging k over the inner dashed line in Figure 4a.

The k measured in Ref. 28 is twice as small as the k measured in Ref. 3 Comparing k between the different simulations and the experiments reveals that RANS agrees best with Ref., 28 and LES agrees best with Ref. 3 Unexpectedly DNS agrees the least with both experimental data sets, predicting a few-fold larger k-values.

The current DNS allows a direct computation of the distribution of ϵ in fully turbulent ST flow without any modeling, while in previously reported ST simulations ϵ needed to be modeled using $k - \epsilon$ (eg., Ref. 29) or using LES (eg., Ref. 4). To the best of our knowledge, only a few research groups published directly measured spatial distributions of ϵ in a ST flow using particle image velocimetry (PIV).[5,30,31] These papers present data as to ϵ outside the turbine swept volume only, while inside this region, where turbulence intensities are most pronounced, ϵ has never been measured so far. In Figure 9b, we compare axial profiles of phase averaged ϵ at $\frac{r}{T} = 0.175$ between the various simulations and two experimental data sets from the literature. These profiles are obtained by averaging ϵ over the outer dashed line in Figure 4a.

The experiments in Figure 9b were conducted using PIV at Reynolds numbers of $Re = 40{,}000$[5] and $Re = 56{,}000$,[31] being an order of magnitude larger than our $Re = 7300$. The tank geometry in the experiments is identical to ours, except for a blade thickness of 0.03 D in Ref. 5 and 0.013 D in Ref. 31 being somewhat smaller than our thickness of 0.04 D. The influence of the Reynolds number and the blade thickness is given in Figure 1b, suggesting a 20% difference in the overall energy dissipation between our simulation and these experiments. The comparison of ϵ in Figure 9b shows that the PIV-data is three times as large as the DNS- and the LES-data, while for RANS the discrepancies are a factor of two.

Assessment of the $k - \epsilon$ model

Figure 10 shows ϵ predicted by DNS, LES, and RANS in the $(\phi = \frac{\pi}{4})$-plane. The ϵ predicted by DNS and LES show two maximum values at $(\frac{r}{T}, \frac{x}{T}) \approx (0.17, \pm 0.02)$, which coincide with the cores of the trailing vortices. RANS does not show such a pair of maximum values. The maximum ϵ in DNS is twice as large as in LES, and four times as large as in RANS. Further away from the turbine at $\frac{r}{T} > 0.2$, DNS and LES predict roughly the same ϵ, while RANS predicts a 50% larger value.

In RANS, the effect of the turbulence on the mean flow is parameterized using a turbulent viscosity model (Eq. 6). The model is based on assuming a similarity between the Reynolds stress $\boldsymbol{R}$ and the mean rate of strain $\overline{\boldsymbol{S}}$. Here, we use the DNS-data to verify this assumption in the ST. For this purpose, we introduce a novel parameter which we denote the eddy-strain alignment parameter

$$\zeta = \frac{\boldsymbol{R} : \overline{\boldsymbol{S}}}{|\boldsymbol{R}||\overline{\boldsymbol{S}}|}. \tag{12}$$

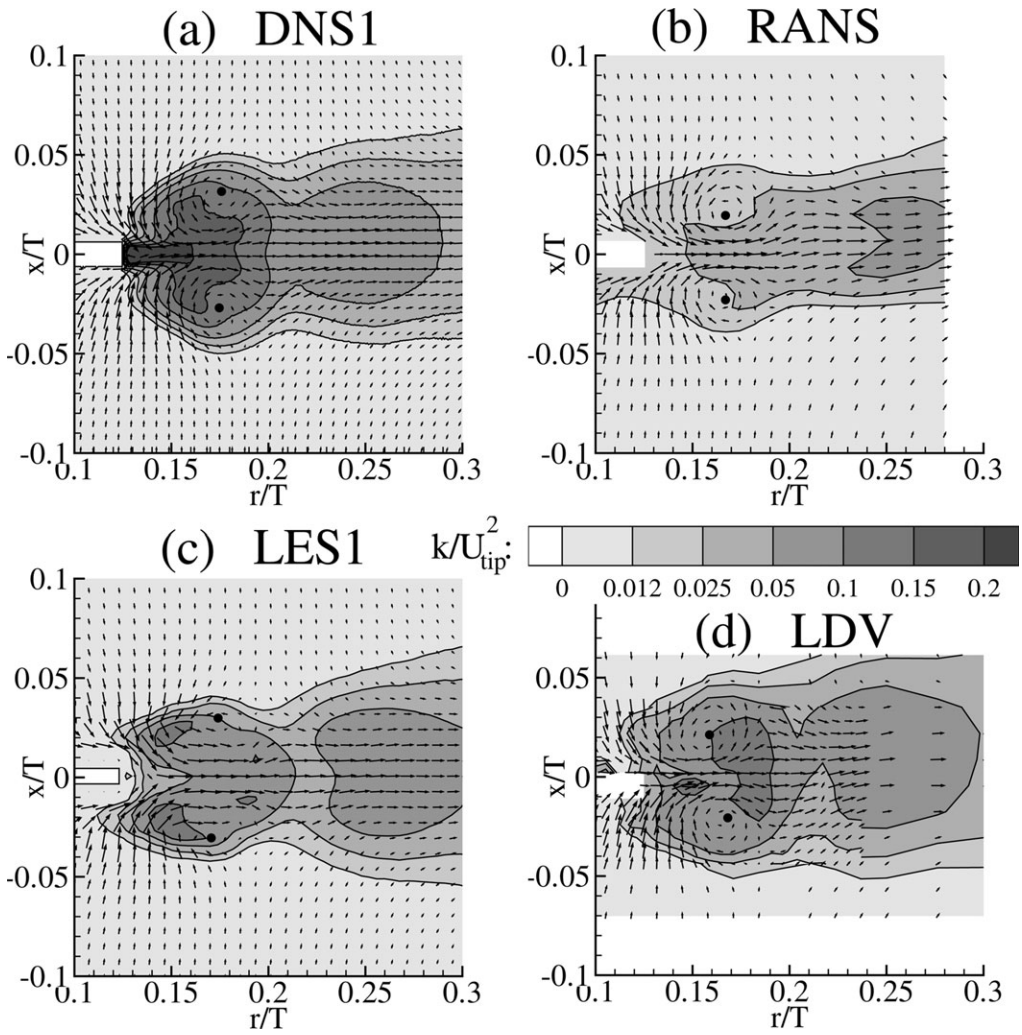

Figure 8. In-plane velocity components and turbulent kinetic energy in the ($\phi = \frac{\pi}{4}$)-plane, predicted by DNS1 (a), RANS of Ref. 6 (b), LES1 (c), and measued using LDV by Ref. 3 (d) The dots indicate the cores of the trailing vortices.

Depending on the relative orientation of $\boldsymbol{R}$ and $\bar{\boldsymbol{S}}$, this parameter can attain values between -1 and $+1$. For $\zeta = 1$, there is a perfect alignment of both the compression as well as the extensional axes of $\boldsymbol{R}$ and $\bar{\boldsymbol{S}}$. For $\zeta = -1$, the extensional axes of $\boldsymbol{R}$ are aligned to the compression axes of $\bar{\boldsymbol{S}}$ and vice versa. In the Appendix, we illustrate the situation for intermediate ζ using a hypothetical, two-dimensional (2-D) example.

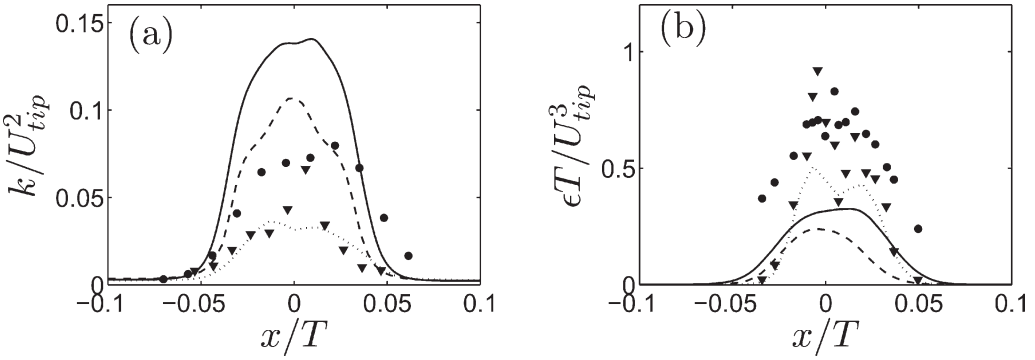

Figure 9. (a) Axial profiles of phase averaged turbulent kinetic energy at $\frac{r}{T} = 0.175$ computed by DNS1 (solid line), LES1 (dashed line), RANS (data from Ref. 6 dotted line), measured with LDV (data from Ref. 3 *Re* $= 7300$, circles), and (data from Ref. 28 *Re* $= 40{,}000$, triangles); (b) axial profiles of phase averaged turbulent energy dissipation at $\frac{r}{T} = 0.225$ computed by DNS1 (solid line), LES1 (dashed line), RANS (data from Ref. 6 dotted line) and measured with PIV (data from Ref. 5 *Re* $= 20{,}000$, circles) and (data from Ref. 31 *Re* $= 56{,}000$, triangles).

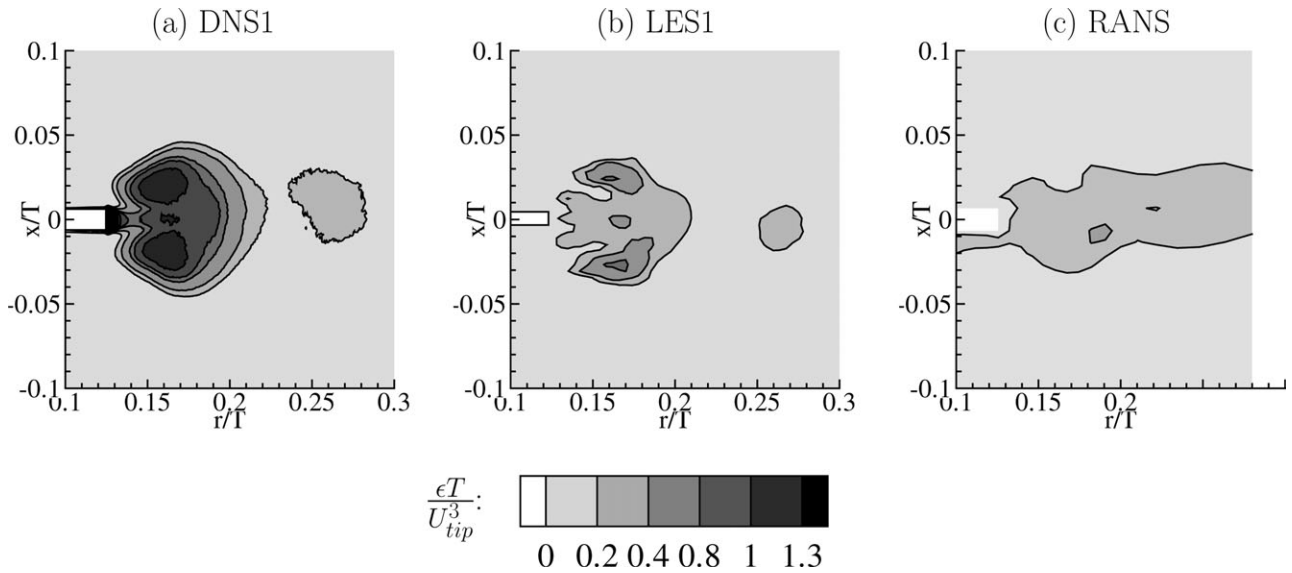

Figure 10. Turbulent energy dissipation in the ($\phi = \frac{\pi}{4}$)-plane predicted by DNS1 (a), LES1 (b), and RANS from Ref. 6 (c)

Figure 11d shows ζ in the ($\phi = \frac{\pi}{4}$)-plane of the ST flow, revealing $\zeta > 0.5$ in the discharge region and $\zeta < 0.5$ outside the stream. According to our 2D model (Eq. A2), $\zeta > 0.5$ corresponds to a relatively small angle $\theta < \frac{\pi}{6}$ between the principal axes of $\boldsymbol{R}$ and $\bar{\boldsymbol{S}}$ in Eq. A1. This means that the similarity assumption between $\boldsymbol{R}$ and $\bar{\boldsymbol{S}}$ is reasonable in the

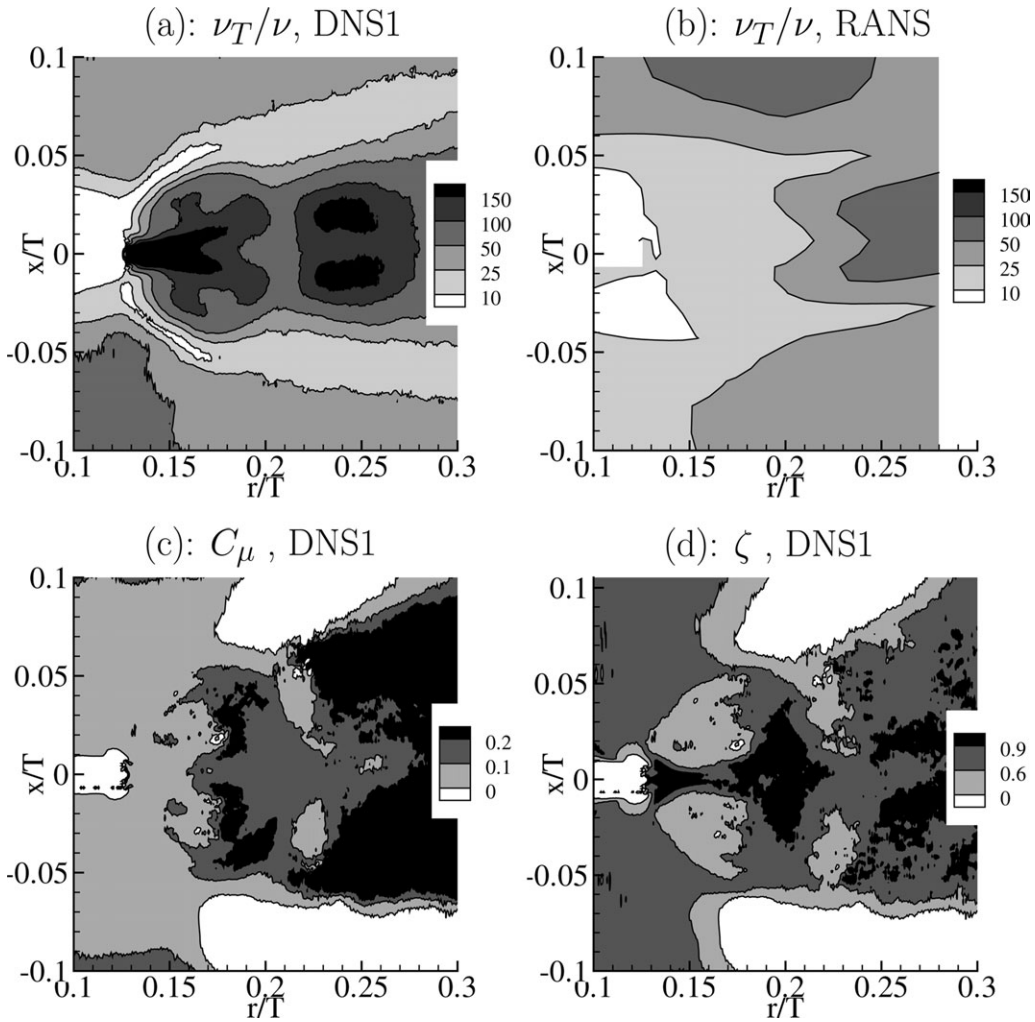

Figure 11. (a) Turbulent viscosity predicted by DNS1; (b) turbulent viscosity predicted by RANS from Ref. 6 (c) Turbulent viscosity parameter predicted by DNS1; (d) Eddy-strain alignment parameter predicted by DNS1.

Data are shown in the ($\phi = \frac{\pi}{4}$)-plane.

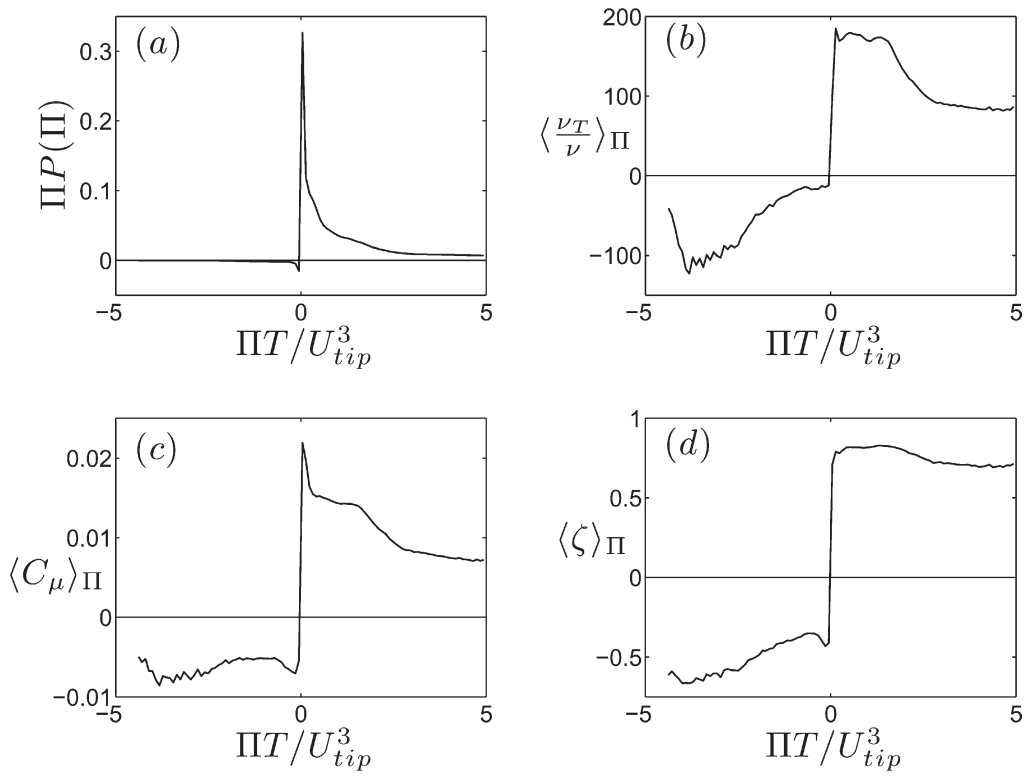

Figure 12. (a) Distribution of turbulent energy production Π; (b) turbulent viscosity conditionally averaged on Π; (c) turbulent viscosity parameter conditionally averaged on Π; (d) Eddy-strain alignment parameter conditionally averaged on Π.

Data are taken from DNS1 in the region $\frac{r}{T} < \frac{1}{3}$ and $|\frac{x}{T}| < \frac{1}{12}$.

discharge stream. Outside the stream on the other hand, $\zeta < 0.5$ and the similarity assumption is disputable.

In Figure 12, we study ζ in a volume V_T around the turbine: $\frac{r}{T} < \frac{1}{3}$ and $|\frac{x}{T}| < \frac{1}{12}$. In particular, we study how ζ is related to the turbulent energy production $\Pi = -\boldsymbol{R}{:}\bar{\boldsymbol{S}}$, describing the transfer of energy from the mean flow to the turbulence. We define $P(\Pi)$ as the probability distribution function of Π, such that the volume averaged Π (over V_T) is given by $\langle \Pi \rangle = \int_{-\infty}^{\infty} P(\Pi)\Pi d\Pi$. Figure 12a shows that the weighted distribution $P(\Pi)\Pi$ peaks at $\Pi T/U_{\text{tip}}^3 \approx 0.1$ and $\approx$90% of $\langle \Pi \rangle$ is due to events within $0 < \Pi T/U_{\text{tip}}^3 < 2$. It further shows that negative Π-events are rare and only $\approx$1% of $\langle \Pi \rangle$ is due to energy transfer from the turbulence to the mean flow.

To study the relation between ζ and Π, we plot in Figure 12d the conditional average of ζ on Π, which is defined as $\langle \zeta \rangle_\Pi = \int_{-\infty}^{\infty} P(\zeta, \Pi)\zeta d\zeta / \int_{-\infty}^{\infty} P(\zeta, \Pi) d\zeta$, where $P(\zeta, \Pi)$ is the joint probability distribution function of the variables ζ and Π. Figure 12(d) shows that $\langle \zeta \rangle_\Pi \approx 0.8$ for $0 < \Pi T/U_{\text{tip}}^3 < 2$, which is the Π-interval that dominates the energy transfer. The large ζ-values indicate strong similarity between $\boldsymbol{R}$ and $\bar{\boldsymbol{S}}$, which confirms the validity of the turbulent viscosity hypothesis.

In RANS, the most commonly used model for the turbulent viscosity is the $k - \epsilon$ model (Eq. 6). The standard value for the turbulent viscosity parameter $C_\mu = 0.09$. We have computed C_μ from the DNS1-data by equating the right hand sides of Eqs. 5 and 6 and taking the double inner product of the result with $\bar{\boldsymbol{S}}$.

$$C_\mu = -\frac{\epsilon\, \boldsymbol{R} : \overline{\boldsymbol{S}}}{k^2\, \overline{\boldsymbol{S}} : \overline{\boldsymbol{S}}} \tag{13}$$

Figure 11c shows C_μ in the ($\phi = \frac{\pi}{4}$)-plane. Inside the discharge stream $C_\mu \sim 0.1$, while outside the stream $C_\mu \lesssim 0.1$. Smaller C_μ outside the stream are due to misalignment between $\boldsymbol{R}$ and $\bar{\boldsymbol{S}}$. Figure 12c shows C_μ, conditionally averaged on Π for $\frac{r}{T} < \frac{1}{3}$ and $|\frac{x}{T}| < \frac{1}{12}$. This figure shows that $\langle C_\mu \rangle_\Pi \approx 0.015$ for $0 < \Pi T/U_{\text{tip}}^3 < 2$. For larger Π, $\langle C_\mu \rangle_\Pi$ approaches a smaller value of $\approx$0.008. The dominating value of $C_\mu \approx 0.015$ is a factor six smaller than the standard $k - \epsilon$ value of 0.09. This result suggests that RANS based on $k - \epsilon$ using $C_\mu = 0.09$ would produce a larger ν_T and consequently a larger k and ϵ than DNS. Surprisingly, the contrary is demonstrated by the comparison between DNS and RANS of k and ϵ in Figures 8 and 10. Furthermore, Figures 11a, b compare ν_T between DNS and RANS, revealing that despite the larger value of C_μ, RANS predicts a significantly smaller ν_T.

Assessment of the Smagorinsky model

Figures 5c, d show that LES1, which is based on the Smagorinsky subgrid model using $C_S = 0.12$, predicts substantially smaller values of k and ϵ in the turbine discharge stream than DNS1. In an attempt to understand these discrepancies, we compute C_S^2 by test filtering $\widehat{\cdots}$ the DNS1-data and computing the associated subfilter stresses without modeling.

$$C_S^2 = \frac{\overline{(-\widehat{\boldsymbol{u}}\widehat{\boldsymbol{u}} + \widehat{\boldsymbol{u}}\widehat{\boldsymbol{u}}) : \widehat{\boldsymbol{S}}}}{\Delta_f^2 \overline{\widehat{\boldsymbol{S}}^3}}. \tag{14}$$

In Eq. 14, the test filter $\widehat{\cdots}$ is applied to the fully resolved DNS1 fields $\boldsymbol{u}$ and $\boldsymbol{S}$, whereas in the dynamics Smagorinsky model (Eq. 10), $\widehat{\cdots}$ is applied to the LES2 fields $\widetilde{\boldsymbol{u}}$ and $\widetilde{\boldsymbol{S}}$. In Eq. 14 the width of the test filter was set equal to six DNS1 grid spacings $\Delta_f = 6\Delta$, which is equal to one LES grid spacing.

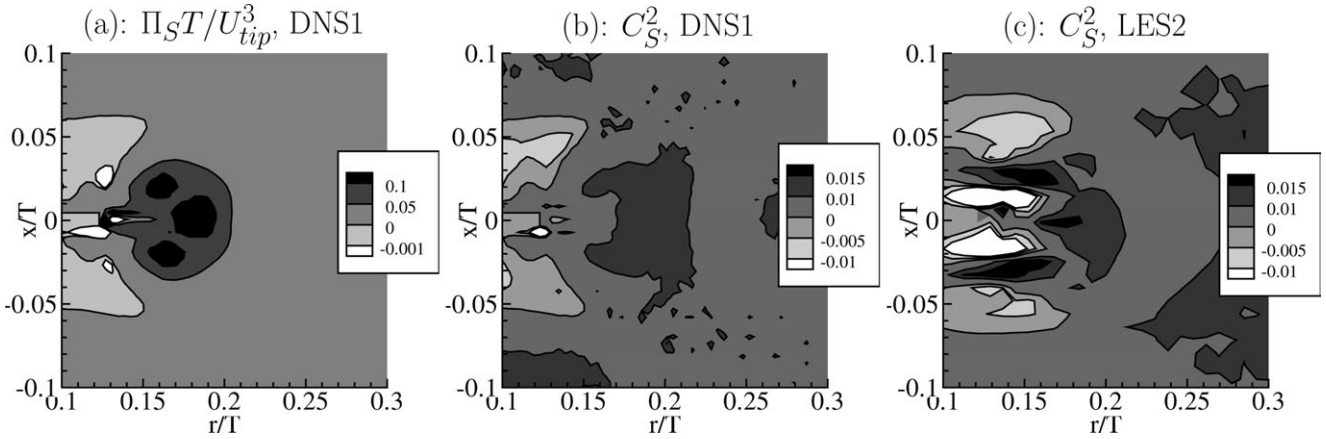

Figure 13. (a) Small eddy energy production in DNS1; (b) Smagorinsky constant squared in DNS1; (c) Smagorinsky constant squared in LES1.

Data are shown in the ($\phi = \frac{\pi}{4}$)-plane.

Figure 13b shows C_S^2 computed from SIM1 in the ($\phi = \frac{\pi}{4}$)-plane. The data show that away from the turbine for $\frac{r}{T} > 0.2$, C_S^2 is rather constant, which indicates that the small eddies behave universally. Apparently, they are largely isotropic and in equilibrium in agreement with the Smagorinsky viscosity hypothesis. Immediately behind the turbine blades for $\frac{r}{T} < 0.2$, however, large variations in C_S^2 are observed. Negative C_S^2 values are observed, which is equivalent to a negative Smagorinsky viscosity ν_e (Eq. 9), reflecting a transfer of energy from small ($<\Delta_f$) to large ($>\Delta_f$) scales, referred to as backscatter (see, eg., Ref. 14). Backscatter reflects misalignment of strain and subgrid stress which is a well known shortcoming of the Smagorinsky model (see, eg., Ref. 13). However, as can be seen in Figure 13a the energy flux between large and small scales $\Pi_S = (-\widehat{\bar{u}\bar{u}} + \widehat{\bar{u}\bar{u}}) : \widehat{\bar{S}} \sim 10^{-3} U_{tip}^3/T$ in the region of backscatter is negligible compared to the $\Pi_S \sim 0.1\ U_{tip}^3/T$ in the trailing vortices.

Figure 14a shows the distribution of Π_S obtained from the DNS1 data in the turbine region: $\frac{r}{T} < \frac{1}{3}$ and $|\frac{x}{T}| < \frac{1}{12}$ using different filter widths $\frac{\Delta_f}{\Delta} = 6$, 18 and 24. The data show that, irrespective of the filter width, the energy transfer is mostly concentrated between $0 < \Pi_S T/U_{tip}^3 < 0.1$. Backscatter ($\Pi_S < 0$) contributes $\approx 1\%$ to the energy transfer. The corresponding C_S^2, conditionally averaged on Π_S is plotted in Figure 14b. Within the dominant region ($0 < \Pi_S T/U_{tip}^3 < 0.1$), $\langle C_S^2 \rangle_\Pi$ is roughly independent of Π_S and increases from 0.01 to 0.02 when the filter width Δ_f is increased from 6Δ to 24Δ.

As C_S^2 is found to be rather constant it is anticipated that the LES of ST flow using the Smagorinsky model can not be improved substantially by dynamically computing C_S. A constant value of $C_S \approx 0.1$ seems to be adequate. To verify this assertion, we have conducted LES2, using the dynamic Smagorinsky model and including the Van Driest wall damping (Eq. 11). The dynamically computed C_S^2 is plotted in the ($\phi = \frac{\pi}{4}$)-plane in Figure 13c. The results are similar to the results obtained by test filtering the DNS1 field in Figure 13b. A universal behavior ($C_S^2 \approx 0.01$) is found away from the turbine ($\frac{r}{T} > 0.15$), while inside the turbine swept volume, variations appear including backscatter. When present on average, backscatter provides stability problems and therefore in LES2, $C_S^2 = 0$ was used whenever the dynamic model predicted $C_S^2 < 0$.

Figure 5 provides a comparison of DNS1, LES1, and LES2 in terms of axial profiles of $\bar{u}$, k, and ϵ at ($\frac{r}{T}$, ϕ) = ($\frac{1}{6}$, $\frac{\pi}{4}$). The figure shows no significant change when switching from the constant Smagorinsky model to the dynamic Smagorinsky with the Van Driest wall damping. Similar to the constant Smagorinsky model, the dynamic Smagorinsky model produces substantially smaller values in k and ϵ in the wake of the turbine blades as compared to DNS. The similar results of LES1 and LES2 indicate that the differences between the

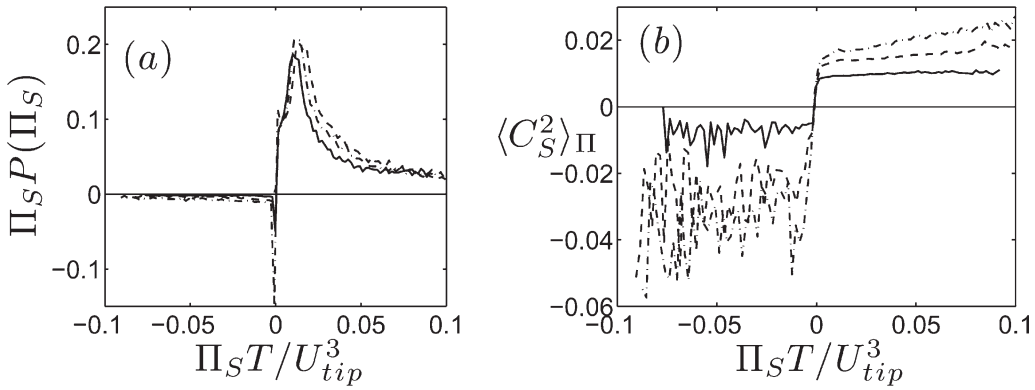

Figure 14. (a) Distribution of small eddy energy production Π_S; (b) Smagorinsky constant squared conditionally averaged on Π_S.

The data are taken from DNS1 in the region $\frac{r}{T} < \frac{1}{3}$ and $|\frac{x}{T}| < \frac{1}{12}$ and the results are shown for three filter widths $\Delta_f/\Delta = 6$ (solid lines), $\Delta_f/\Delta = 18$ (dashed lines), and $\Delta_f/\Delta = 24$ (dash-dotted lines).

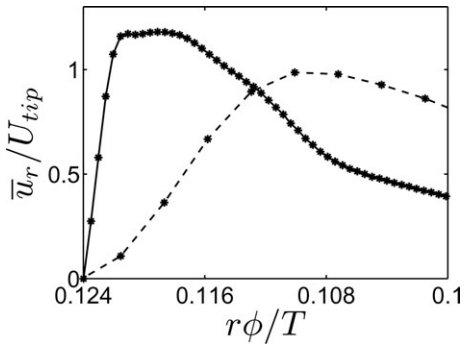

Figure 15. Comparison of Reynolds averaged radial velocity at $(\frac{x}{T}, \frac{r}{T}) = (\frac{21}{60}, \frac{1}{8})$, predicted by DNS1 (solid line) and LES1 (dashed line).

present LES and DNS are not due to the specific values of C_S, but originate from other shortcomings in the LES.

One source of error in the present LES is the related to our immersed boundary method to enforce the no-slip condition on the moving blades. It is known that this method results in an apparent increase in the hydrodynamic diameter of the no-slip objects.[32] This increase is in the order of a grid-spacing Δ, which is small compare to the blade thickness t in the DNS ($\Delta/t = 0.05$) but is more substantial in the LES ($\Delta/t = 0.3$).

Another and probably more severe source of error in the present LES is due to the under-resolved velocity gradient on the turbine surface. To study this, we have used the DNS-data to calculate the shear stress on the turbine blades and computed the corresponding viscous length scale. Based on this, we have estimated the grid spacing in the LES to be approximately equivalent to 20 viscous length scales obviously, such a grid spacing is too large to correctly capture the velocity profile in the viscous sublayer. The effect of this under-resolution is illustrated in Figure 15, where we compare DNS1 and LES1 in predicting the Reynolds averaged radial velocity profile normal to the blade. The profiles are plotted as functions of ϕ and are located at $(\frac{x}{T}, \frac{r}{T}) = (\frac{21}{60}, \frac{1}{8})$. This curve is located at one quarter blade height above the edge of the disk. In the plot, the blade surface is located at $\phi r/T = 0.124$. The DNS shows a very steep gradient in the viscous sublayer attached to the blade. Clearly, the LES cannot resolve this gradient. Instead the LES predicts a much weaker gradient and this effects the shape of the profile, also outside the viscous sublayer.

Discussion and Conclusion

We have conducted DNS and LES of the turbulent flow inside a ST at a Reynolds number of $Re = 7300$. To verify whether the simulation was fully resolving all scales, we have computed the Kolmogorv length scale. It was found that the minimum Kolmogorov length scale in the wake of the turbine blades is somewhat smaller than the grid spacing. To further study the grid resolution issue, we visualized the instantaneous vorticity, showing smooth structures on all length scales, suggesting a well-resolved turbulent flow field. Furthermore, we demonstrated a fair agreement of ϵ predicted by the DNS and that predicted by a second DNS, with a coarser resolution. Although we are not 100% certain of having fully resolved the smallest eddies behind the blades, the present DNS provides a significant step forwards.

We compared DNS and LES to RANS, LDV and PIV-data from the literature. The DNS and the experiments agree within a few percent in terms of $\overline{\boldsymbol{u}}$, while in close proximity to the turbine blades, differences in k and ϵ are as large as 50%. At certain locations, the LES and RANS agree better with the experimental data than DNS in terms of k and ϵ. This unexpected observation suggests that more numerical and experimental work is required to reliably determine ϵ close to the turbine.

The main purpose of this work was to use the DNS-data to validate the fundamental assumptions underlying LES and RANS, and to study how these models perform in predicting ST flow. In this context, we have analyzed the Reynolds stress $\boldsymbol{R}$ obtained by Reynolds averaging the DNS flow field. The turbulent viscosity hypothesis is validated by showing strong alignment between $\boldsymbol{R}$ and the mean strain rate $\bar{\boldsymbol{S}}$. The DNS predicted that the dominant values of the turbulent viscosity parameter lie within the range: $0.008 < C_\mu < 0.02$, which is an order of magnitude smaller than the standard value $C_\mu = 0.09$. The RANS simulation however predict a substantially smaller ν_T (and associated k and ϵ) than the DNS. These differences may therefore not be due to shortcomings in the turbulent viscosity hypothesis, but rather may be related to inconsistencies in the phenomenological transport equations for k and ϵ. This is to be investigated in greater detail.

We also evaluated the performance of LES based on the Smagorinsky subgrid model. Away from the turbine blades, good agreement with DNS was found, while inside the turbine swept volume k and ϵ were predicted 50% smaller than by DNS. These differences did not reduce by dynamically computing the Smagorinsky constant nor by applying the Van Driest wall damping in the LES. By filtering the DNS-data, we determined the optimal Smagorinsky constant as $C_S \approx 0.1$, which is identical to the dynamically computed value in the LES. This suggests that the discrepancies between DNS and LES are not linked to shortcomings in the Smagorinsky model. These discrepancies are most likely due to the under-resolved velocity gradients in the LES near the solid walls. It is anticipated that an underestimation of the wall shear stress results in an underestimation of the turbulent energy production, which could explain the observed underestimated values for k and ϵ in the LES. These issues might be improved by adopting so-called hybrid RANS-LES, which is known to provide better predictions of the wall shear stress as compared to LES.[14,33,34]

Acknowledgments

This work was sponsored by the Stichting Nationale Computerfaciliteiten (National Computing Facilities Foundation NCF) for the use of supercomputer facilities, with financial support from the Nederlandse Organisatie voor Wetenschappelijk Onderzoek (Netherlands Organization for Scientific Research, NWO).

The authors are grateful to Prof. Jos Derksen of the University of Alberta for providing us with the LB code and to Jane Pearson of the ANSYS Coorporation for providing us with the RANS-data and to Prof. Sankaran Sundaresan of the University of Princeton for helpful discussions.

Literature Cited

1. Yianneskis M, Popiolek Z, Whitelaw JH. An experimental study of the steady and unsteady flow characteristics of stirred reactors. *J Fluid Mech*. 1987;175:537–555.
2. Bakker A, Van den Akker HEA. Single-phase flow in stirred reactors. *Chem Eng Res Des*. 1994;72A:583–593.
3. Schäfer M, Hofken M, Durst F. Detailed LDV measurements for visualization of the flow field within a stirred-tank reactor equipped with a Rushton turbine. *Chem Eng Res Des*. 1997;75:729–736.
4. Derksen JJ, Van den Akker HEA. Large eddy simulations on the flow driven by a Rushton turbine. *AIChE Journal*. 1999;45:209–221.

5. Baldi S, Yianneskis M. On the quantification of energy dissipation in the impeller stream of a stirred vessel from fluctuating velocity gradient measurements. *Chem Eng Sci*. 2004;59:2659–2671.
6. Hartmann H, Derksen JJ, Montavon C, Pearson J, Hamill IS, Van den Akker HEA. Assessment of large eddy and rans stirred tank simulations by means of LDA. *Chem Eng Sci*. 2004;59:2419–2432.
7. Sommerfeld M, Decker S. State of the art and future trends in CFD simulations of stirred vessel hydrodynamics. *Chem Eng Technol*. 2004;27:215–224.
8. Joshi JB, Nere NK, Rane CV, Murthy BN, Mathpati CS, Patwardhan AW, Ranade VV. CFD simulation of stirred tanks: comparison of turbulence models. Radial flow impellers. *Can J Chem Eng*. 2011; 89:23–82.
9. Wilcox DC. *Turbulence Modeling for CFD*. DCW Industries: La Canada, 1993.
10. Montante G, Lee KC, Brucato A, Yianneskis M. Numerical simulations of the dependency of flow pattern on impeller clearance in stirred vessels. *Chem Eng Sci*. 2001;56:3751–3770.
11. Van den Akker HEA. The details of turbulent mixing process and their simulation. *Adv Chem Eng*. 2006;31:151–229.
12. Sagaut P. *Large Eddy Simulation for Incompressible Flows*. Springer: Berlin: 2001.
13. Liu S, Meneveau C, Katz J. On the properties of similarity subgrid-scale models as deduced from measurements in a turbulent jet. *J Fluid Mech*. 1994;275:83–119.
14. Piomelli U, Balaras E. Wall-layer models for large eddy simulations. *Ann Rev Fluid Mech*. 2002;34:349–374.
15. Bartels C, Breuer M, Durst F. *Comparison between direct numerical simulation and* k − ϵ *prediction of the flow in a vessel stirred by a Rushton turbine*. HEA Van den Akker, JJ Derksen. Eds. In: *Proceedings of the 10th European conference on mixing*, 2000; Delft, The Netherlands. pp 239–243.
16. Bartels C, Breuer M, Wechsler K, Durst F. Computational fluid dynamics applications on parallel-vector computers: computations of stirred vessel flows. *Comput Fluids*. 2002;31:69–97.
17. Verzicco R, Fatica M, Iaccarino G, Orlandi P. Flow in an impeller-stirred tank using an immersed-boundary method. *AIChE J*. 2004;50: 1109–1118.
18. Sbrizzai F, Lavezzo V, Verzicco R, Campolo M, Soldati A. Direct numerical simulation of turbulent particle dispersion in an unbaffled stirred-tank reactor. *Chem Eng Sci*. 2006;61:2843–2851.
19. Bates RL, Fondy PL, Corpstein RR. Examination of some geometric parameters of impeller power. *Ind Eng Chem Process Des Dev*. 1963;2:310–314.
20. Smagorinsky J. General circulation experiments with the primitive equations. *Mon Weather Rev*. 1963;91:99–164.
21. Germano M, Piomelli U, Moin P, Cabot WH. A dynamic subgrid-scale eddy viscosity model. *Phys Fluids A*. 1991;3:1760–1766.
22. Yoshizawa A, Horiuti K. A statistically-derived subgrid-scale kinetic energy model for the large-eddy simulation of turbulent flows. *J Phys Soc Jpn*. 1985;54:2834–2839.
23. Somers JA. Direct simulation of fluid flow with cellular automata and the lattice-Boltzmann equation. *Appl Sci Res*. 1993;51:127–133.
24. Lu Z, Liao Y, Qian D, McLaughlin JB, Derksen JJ, Kontomaris K. Large eddy simulations of a stirred tank using the lattice Boltzmann method on a nonuniform grid. *J Comput Phys*. 2002;181:675–704.
25. Rohde M, Kandhai D, Derksen JJ, Van den Akker HEA. A generic, mass conservative local grid refinement technique for lattice-Boltzmann schemes. *Int J Numer Method Fluids*. 2006;51:439–468.
26. Van Driest ER. On turbulent flow near a wall. *J Aerosol Sci*. 1956;23:1007–1011.
27. Chapple D, Kresta SM, Wall A, Afacan A. The effect of impeller and tank geometry on power number for a pitched blade turbine. *Inst Chem Eng*. 2002;80:364–372.
28. Lee KC, Yianneskis M. Turbulence properties of the impeller stream of a Rushton turbine. *AIChE J*. 1998;44:13–24.
29. Ng K, Yianneskis M. Observations on the distribution of energy dissipation in stirred vessels. *Chem Eng Res Des*. 2000;78:334–341.
30. Sharp KV, Adrian RJ. PIV study of small-scale flow structure around a Rushton turbine. *AIChE J*. 2001;47:766–778.
31. Escudié R, Liné A. Experimental analysis of hydrodynamics in a radially agitated tank. *AIChE J*. 2003;49:585–603.
32. Ten Cate A, Nieuwstad CH, Derksen JJ, Van den Akker HEA. Particle imaging velocimetry experiments and lattice-boltzmann simulations on a single sphere settling under gravity. *Phys Fluids* 2002; 14:4012–4025.
33. Kenjereš S, Hanjalič K. LES, T-RANS and hybrid simulations of thermal convection at high Ra numbers. *Int J Heat Fluid Flow*. 2006;27:800–810.
34. Gimbun J, Rielly CD, Nagy ZK, Derksen JJ. Detached eddy simulation on the turbulent flow in a stirred tank. *AIChE J*. 2011 In press.

Appendix

Eddy-strain alignment parameter in two dimensions

Here, we illustrate the behavior of ζ (Eq. 12) in a 2-D flow field. In this flow field, we assume that $\bar{\boldsymbol{S}}$ has a positive eigenvalue λ in the $\boldsymbol{e}_x$-direction (extensional axis) and a negative eigenvalue $-\lambda$ in the $\boldsymbol{e}_y$-direction (compression axis). Furthermore, we assume that $\boldsymbol{R}$ has a positive eigenvalue κ in the $\boldsymbol{e}'_x$-direction and a negative eigenvalue $-\kappa$ in the $\boldsymbol{e}'_y$-direction. Here, $\boldsymbol{e}'_x = \cos(\theta)\boldsymbol{e}_x + \sin(\theta)\ \boldsymbol{e}_y$ and $\boldsymbol{e}'_y = -\sin(\theta)\boldsymbol{e}_x + \cos(\theta)\boldsymbol{e}'_y$. These directions are obtained by a rotation of $\boldsymbol{e}_x$ and $\boldsymbol{e}_y$ over θ.

$$\overline{\boldsymbol{S}} = \lambda \begin{pmatrix} 1 & 0 \\ 0 & -1 \end{pmatrix},\ \boldsymbol{R} = \kappa \begin{pmatrix} \cos^2(\theta) - \sin^2(\theta) & 2\cos(\theta)\sin(\theta) \\ 2\cos(\theta)\sin(\theta) & \sin^2(\theta) - \cos^2(\theta) \end{pmatrix}. \tag{A1}$$

Inserting Eq. (A1) in Eq. 12 gives

$$\zeta = \cos(2\theta), \tag{A2}$$

showing maximum alignment ($\zeta = 1$) for $\theta = \pi(1 + 2n)$, minimum alignment ($\zeta = -1$) for $\theta = \frac{\pi}{2}(1 + 2n)$, and intermediate alignment ($\zeta = 0$) for $\pi = \frac{\pi}{4}(1 + 2n)$, with n an integer.

Manuscript received Nov. 3, 2011, and revision received Dec. 29, 2011.